PROCEEDINGS OF SPIE

SPIEDigitalLibrary.org/conference-proceedings-of-spie

Investigation of light-emission and avalanche-current mechanisms in PureB SPAD devices

Lis K. Nanver, M. Krakers, T. Knezević, A. Karavidas, I. Boturchuk, et al.

Lis K. Nanver, M. Krakers, T. Knezević, A. Karavidas, I. Boturchuk, V. Agarwal, R. J. E. Hueting, S. Dutta, A. J. Annema, "Investigation of light-emission and avalanche-current mechanisms in PureB SPAD devices," Proc. SPIE 11043, Fifth Conference on Sensors, MEMS, and Electro-Optic Systems, 1104306 (24 January 2019); doi: 10.1117/12.2501598

Event: Fifth Conference on Sensors, MEMS, and Electro-Optic Systems, 2018, Skukuza, South Africa

SPIE.

Downloaded From: https://www.spiedigitallibrary.org/conference-proceedings-of-spie on 1/29/2019 Terms of Use: https://www.spiedigitallibrary.org/terms-of-use

Investigation of light-emission and avalanche-current mechanisms in PureB SPAD devices

Lis K. Nanver[1,2], M. Krakers[1], T. Knezević[1,3], A. Karavidas[1], I. Boturchuk[1,4], V. Agarwal[1], R.J.E. Hueting[1], S. Dutta[1], A.J. Annema[1]

[1]MESA+ Institute for Nanotechnology, University of Twente, Enschede, The Netherlands
[2]Dept. Mechanical and Manufacturing Engineering, Aalborg University, Aalborg, Denmark
[3]Micro and Nano Electronics Laboratory, University of Zagreb, Croatia
[4]Interdisciplinary Nanoscience Center - INANO-Fysik, Aarhus University, Aarhus, Denmark

ABSTRACT

The light emission from silicon PureB photodiodes was investigated in both forward- and avalanche-mode operation and correlated to the presence of process-dependent defects that influence the reverse *I-V* characteristics. As opposed to "defect-free" diodes with low dark currents and abrupt breakdown behavior, the diodes with defects had higher current levels and light-emitting spots appearing at voltages far below the breakdown voltage otherwise set by the implemented doping profiles. The role of such defect-related behavior for the application of the photodiodes as single-photon avalanche diodes (SPADs) and avalanche-mode light-emitting diodes (AMLEDs) is assessed in connection with the recent demonstration of these basic devices as both the light-emitting and light-detecting elements in optocoupler circuits integrated in CMOS for data transmission purposes.

Keywords: avalanche breakdown, defects, light-emitting diode (LED), Pure boron, silicon, single-photon avalanche diode (SPAD)

1. INTRODUCTION

There is an interest in realizing high-speed optical links on-chip in CMOS circuits by integrating silicon (Si) photodiodes that can be used for both light emission and light detection. For such on-chip optocoupling a number of reports have underlined the advantages of using avalanche-mode light-emitting diodes (AMLEDs) rather than forward-mode LEDs (FMLEDs) as the light source [1-4]. The low junction capacitance and carrier drift associated with reverse biasing of the diode means that AMLEDs are fast. For example, small signal modulation speed in the range of tens of GHz has been reported [5]. There are also reports that the coupling efficiency between an AMLED and a Si photodiode detector (PD) is higher than when the same LED is operated in forward mode [6], due to the stronger overlap between the emission spectrum of Si AMLEDs and the spectral responsitivity of Si PDs [1, 7]. Nevertheless, the efficiency of light emission from Si AMLEDs is very low, in the range of 10^{-5} [1]. Therefore, for light detection a very sensitive PD is required. It has recently been demonstrated that this can be achieved by using Si single-photon avalanche diodes (SPADs) that work in Geiger mode: both the SPAD and the AMLED were integrated in a standard 140 nm silicon-on-insulator CMOS technology, and a low-power monolithically-integrated optical transmitter was successfully realized [8]. The functioning of both AMLEDs and SPADs are dependent on low dark currents and a well-defined avalanche breakdown [9]. However, there are a number of differences in the overall requirements for optimal functioning of the two types of devices. Recent studies using photodiodes fabricated in pure boron (PureB) technology were directed towards gaining a better understanding of the differences in avalanching mechanisms that are important for the functioning of SPADs/AMLEDs [10, 11].

This paper includes an overview of the experimental PureB diodes that were used in these earlier studies. In [12] an analytical model was developed to describe the light emission spectrum from abrupt silicon p^+n junctions operated in avalanche mode. In this study, advantage was taken of the fact that for photodiodes with PureB-only light-entrance

Fifth Conference on Sensors, MEMS, and Electro-Optic Systems, edited by Monuko du Plessis,
Proc. of SPIE Vol. 11043, 1104306 · © 2019 SPIE · CCC code: 0277-786X/19/$18 · doi: 10.1117/12.2501598

Downloaded From: https://www.spiedigitallibrary.org/conference-proceedings-of-spie on 1/29/2019
Terms of Use: https://www.spiedigitallibrary.org/terms-of-use

windows the light is generated within a few nanometer of the diode surface, thus allowing light to escape from the Si even in the ultraviolet (UV) spectral range. To obtain such extremely shallow p^+-n-like junctions, PureB diodes are fabricated by low-temperature deposition of a layer of pure boron. This forms a p-type region that in many ways behaves like a conventional deep boron diffused p-region. However, bulk doping of the Si cannot explain the attractive electrical properties, which instead have been ascribed to the creation of a monolayer of negative fixed charge at the Si interface that in turn attracts holes to the interface while effectively suppressing electron injection from the n-region [13, 14]. This, combined with the damage-free processing method, results in low dark currents. Applications requiring the detection of beams with very low penetration depths in Si, such as advanced semiconductor lithography and electron microscopy, have driven the development of PureB technology [13, 15]. An additional differentiating factor has been the high stability and robustness of both the boron layer itself and the B-Si interface layer upon exposure to high-dose irradiation with light in the wavelength range from 1 nm to 400 nm as well as to low-energy electrons. Moreover, the PureB process used in the present study is front-end CMOS compatible. Today, there is a focus on developing back-end CMOS compatible PureB process modules for coating backside illuminated imagers [16, 17]. In particular, there is a strong technology push to develop medical CMOS imagers for the 300 nm - 400 nm wavelength range. This is also one of the applications where, for high resolution imaging arrays, SPADs are gaining ground [18, 19].

The quality of the PureB photodiodes used in the SPAD/AMLED studies [10-12], varied from exceptionally good "SPAD-quality" diodes, i.e., characterized by low dark count rates (DCRs) and well-defined abrupt breakdown, to devices with defects that appeared as light-emitting spots at voltages far below the breakdown of the ideal "defect-free" devices. The defect density depended on the exact process flow, but for the studied devices it was low, never more than about 1 per μm^2. The impact on the reverse characteristics of the devices was, however, often significant. In this paper a more detailed examination was performed on the relationship between defects, breakdown characteristics, and light-emission for both modes of operation, forward-mode (FM) and avalanche-mode (AM), for a large variety of devices with different geometries and realized under different process conditions.

SPAD-quality PureB devices were previously presented in [20-23]. They were processed with a PureB-only 3-nm-thin light-entrance window and very low leakage current up to an abrupt breakdown at 14 V reverse bias. They were characterized with respect to DCR, photon detection probability (PDP) and afterpulsing. In particular, they were demonstrated to perform well in the ultraviolet wavelength range down to 330 nm [21] and for the detection of low-energy electrons down to 200 eV [23]. They displayed high sensitivity and very low dark count rates, down to 5 Hz at room temperature for a low excess bias of 0.5 V.

In [10, 11] the breakdown mechanism was investigated making use of PureB devices with a significant but low defect count that allowed breakdown characteristics with an abrupt transition between a low dark current and avalanche breakdown. Voltage dependent random telegraph signal (RTS) noise phenomena were shown to determine the steep current-voltage (*I-V*) dependency in avalanche [10]. Using a time-domain analysis (TDA), the statistical properties of these RTS phenomena were determined and an accurate experimental definition of breakdown voltage (*BV*) was proposed based

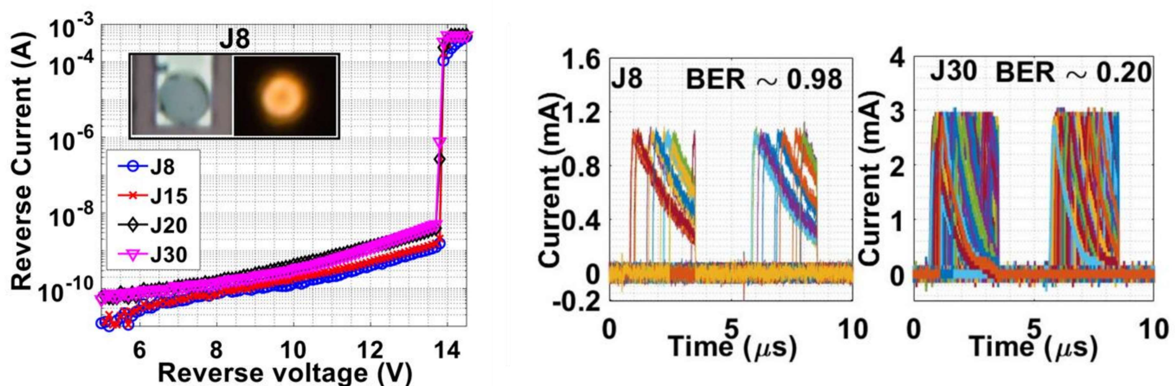

Figure 1. Results report in [11]. Left: *I-V* characteristics of PureB AMLEDs with circular geometry and diameters of 8 μm, 15 μm, 20 μm, and 30 μm. In the inset a microscope image of the 8-μm diodes is shown beside an image of the light emission for biasing at a reverse current of 1 mA. Right: Measured transient waveforms of the AMLED current at a reverse bias of 17.6 V for the 8- μm and 30-μm devices indicating the very high bit-error-rate for the 8-μm diode.

Downloaded From: https://www.spiedigitallibrary.org/conference-proceedings-of-spie on 1/29/2019
Terms of Use: https://www.spiedigitallibrary.org/terms-of-use

on the RTS analysis. Moreover, a value for self-sustaining avalanche current in diodes was parametrically determined, which could be used for an accurate design of quenching-and-recharge circuits (QRCs) for SPADs.

In [11] the data transmission capabilities of the PureB AMLEDs were examined using a pulse position modulation scheme, with which the bit-error rate (BER) and the jitter in the transmitted data were determined. The results were correlated to the leakage current and multiplication noise of the AMLEDs, that increased with the anode area due to the area-related increase in the number of defects. An elevated leakage current was shown to improve the triggering rate of avalanching, thereby reducing the BER and jitter as illustrated in Fig. 1. Conversely, sensitive SPADs should be designed to allow biasing past the BV without triggering an avalanche. In the absence of active defects, an avalanche event can be accorded to triggering even by a single incoming photon. For AMLED operation, a trade-off needs to be found between high triggering rate and the two methods of achieving this: high dark currents or high over-biasing of the junction beyond the BV. Both methods enhance the triggering rate but at the cost of power consumption. Otherwise, the latter could always be used to obtain a high triggering rate even for SPAD-quality devices. This paper elaborates on the viability of incorporating defects as part of the fabrication process for obtaining sufficient carrier injection for fast triggering of AMLEDs.

2. EXPERIMENTAL PROCEDURES

2.1 PureB photodiode fabrication and design

A schematic cross section of the basic process flow used to fabricate the PureB photodiodes is shown in Fig. 2a. The starting substrates were p-type (100) 2-5 Ω-cm Si wafers. Electrical isolation between the individual devices was enhanced by implanting and annealing an n^+-layer before depositing a 1.0-µm-thick almost intrinsic n-type epitaxial layer. To further ensure a low series resistance, the n^+-layer was contacted by implanted n^+ plugs. To obtain a high fill factor and avalanche breakdown away from the diode perimeter, the BV was set by an n-enrichment region created by implanting phosphorus through a 30-nm thermal silicon oxide, first at 40 keV to a dose of 1×10^{12} cm^{-2} and then at 300 keV to a dose of 5×10^{12} cm^{-2}. A 300-nm low-pressure chemical-vapor deposited silicon oxide was then deposited and the implants were annealed at 950°C for 20 min. The windows to the Si defining the anode area were opened and covered with a PureB layer to a thickness of about 3 nm as described in [20]. The deposition temperature was 700°C, and followed by a drive-in for 1 min

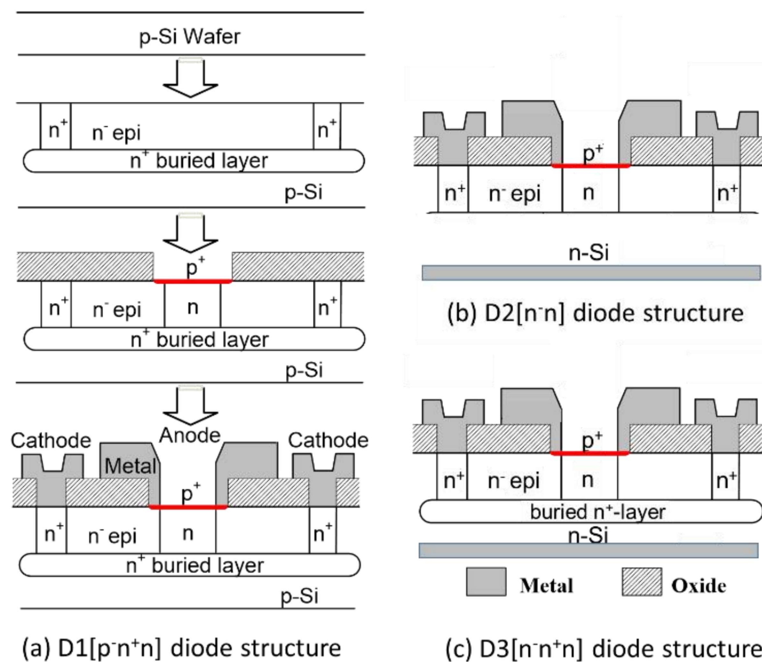

Figure 2. Cross-sectional schematics of the 3 different diode structures under investigation. (a) The basic process flow for the fabrication of PureB SPADs with n^+ plugs to a buried n^+-layer on a p-type Si substrate, denoted D1[p^-n^+n] diodes in Table 1; (b) the D2[n^-n] and (c) D3[n^-n^+n] diode, both processed on n-type substrates without and with a buried n^+-layer, respectively.

Downloaded From: https://www.spiedigitallibrary.org/conference-proceedings-of-spie on 1/29/2019
Terms of Use: https://www.spiedigitallibrary.org/terms-of-use

at 850°C. This resulted in doping of the surface Si giving a junction depth of about 15 nm and a sheet resistance of the p-type anode region of 1.7 kΩ/sq. Finally, aluminum layers were deposited on both sides of the wafer and patterned to form the interconnect contacts to the cathode and the perimeter of the anode, leaving the central anode region with an PureB-only light-entrance window.

As illustrated in Figs. 2b and 2c, process variations were implemented by using n-type 2-5 Ω-cm Si substrates and for some devices the buried n^+-layer was omitted. Moreover, the 40 keV part of the n-enhancement implant was varied by increasing the doses to 3.5×10^{12} cm^{-2}, 6×10^{12} cm^{-2}, and 8.5×10^{12} cm^{-2}. This implant sets the depletion width over the anode junction that determines the *BV*, independent of the presence of the buried n^+-layer, the up-diffusion of which could possibly increase the critical doping level. Using *C-V* doping-profiling techniques on devices with and without the n^+-layer, it was carefully checked that this was not the case. An unintentional process variation originated from a small contamination of the n-substrate surface that occurred during the processing of the buried n^+-layer. In this process run a random distribution of defects was identified electrically by monitoring of a parallel run containing vertical NPN bipolar transistors. Across-the-wafer measurements of the *I-V* characteristics of these bipolar transistors displayed an abnormally high number of emitter-collector (E-C) shorts. Such E-C shorts are typically measured when stacking faults, often called "pipelines" in this respect, are formed during the epi growth causing short-circuiting between the emitter and collector through the narrow base region. In diodes, such pipelines will not short-circuit the p-n junction but they are a source of generation-recombination (g-r) centers that can increase the dark current and reduce the effective *BV*. An overview of the different PureB photodiodes that were studied here is given in Table 1, along with the main process parameters and diode characteristics. References to previous experimental studies using these devices are also listed.

In the layout, several rows of photodiodes were designed with both circular and rectangular anode geometries, an overview of which are given in Fig. 3. In addition, the parameters defining the n-enhancement and photosensitive area are shown schematically. At the outer perimeter of the PureB anode a ring of aluminum, of the same width as the implicit guard ring, is left standing in order to provide connection to the rest of the interconnect layer.

Table 3. Overview of the processing parameters, ideal breakdown voltage, and relative defect-density-related avalanching events, for the PureB diodes treated in his paper along with references to previous studies of the same diodes.

diode type	substrate	buried n^+-layer	40 keV n-implant (atoms-cm^2)	ideal breakdown voltage(V)	defect-related avalanching	referenced in
D1[p^-n^+n]	p-type	yes	1×10^{12}	14.0	-	[20-23]
			3.5×10^{12}	12.5	-	[21], [22]
			6×10^{12}	11.8	-	[21], [22]
			8.5×10^{12}	10.9	+	[21], [22]
D2[n^-n]	n-type	no	1×10^{12}	14.0	+	[10-12]
			3.5×10^{12}	12.5	+	
			6×10^{12}	11.8	++	
			8.5×10^{12}	10.9	++	
D3[n^-n^+n]	n-type	yes	1×10^{12}	14.0	+++	[13]

Downloaded From: https://www.spiedigitallibrary.org/conference-proceedings-of-spie on 1/29/2019
Terms of Use: https://www.spiedigitallibrary.org/terms-of-use

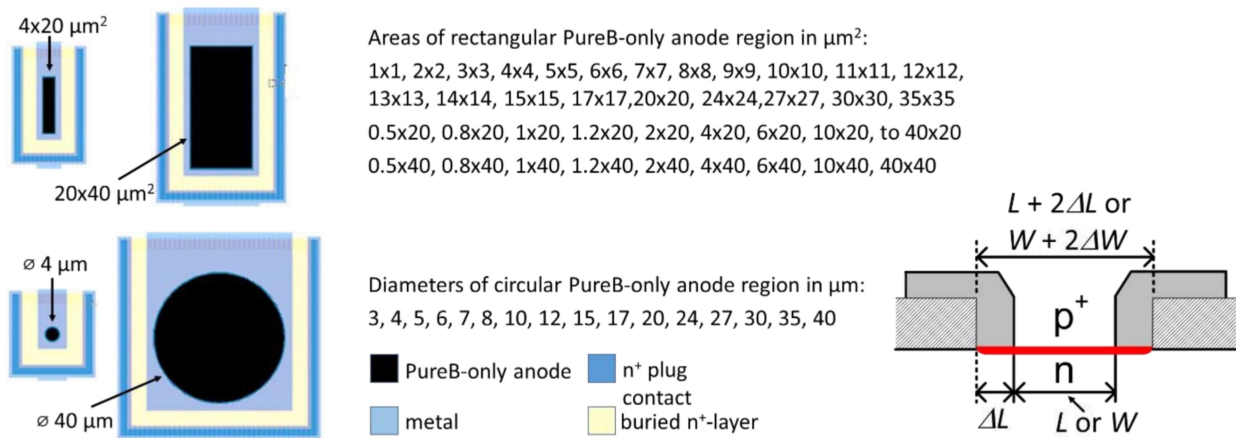

Figure 3. Top view of the PureB diode layouts for examples of small and large, rectangular and circular diodes; with a specification of the available anode areas. On the right, a schematic cross section is shown of the metal contacting scheme of PureB diodes with an n-enrichment implantation. The L and W refer to the length and width, respectively, of devices with a rectangular anode. For all the available diodes, a ΔL = 0.5 μm, 1.0 μm and 1.5 μm was implemented.

2.2 Diode biasing and light-emission measurements

The light emitted from the PureB diodes to be compared as LEDs, were monitored in 4 different ways. Firstly, the emitted light-spectra were monitored with spectrometers. The avalanche-mode spectra were measured with an ADC-1000-U spectrometer from Avantes that was used with a 50 μm multi-mode optical fiber. The spectral line width (resolution) was ~ 0.4 nm and the integration time was chosen to be 16 s. In forward mode, the spectrometer was swapped for an AVASPECUV/VIS/NIR Dual Channel BroadBand spectrometer allowing measurements up to 1800 nm. The capture efficiencies of the spectrometers were unknown so only the normalized spectra are shown in Fig. 4. Also included is the previously reported external quantum efficiency (EQE) of PureB photodiodes with a 3 nm PureB-only light-entrance windows [25]. From this the internal quantum efficiency (IQE) was calculated by assuming that the reflectance from the diode surface was identical to that of bare Si. The good overlap of the visual light emission in AM with the PD responsivity is evident. As opposed to this, the overlap with the FM spectrum is quite small but since the intensity can be as much as 2 decades higher than in AM, it is not evident that the light detected by a Si PD will be less than it is for AM operation of the LED. To make a quantitative comparison between the light emission from the different LED structures and operation modes, a set-up was built to detect the light with large PureB PDs as illustrated in Fig. 5. The LEDs were biased on-wafer using a wafer prober and a Keithley parameter analyser that also was used for biasing the PD via cables. The fabrication of the large PD was described in [16]. They could be placed at 2 different positions on the microscope. In one series of measurements the PD-A positioning of the PD in one of the two oculars was used. Half the LED light reaching the objective of the microscope could then be observed in the other ocular. In this way, accurate positioning of each LED was possible so that the full image of the LED was always focused on the light-sensitive surface of the PD. The light was gathered in a 20× lens with diameter 25.2 mm placed 20 mm above the LED, and the optical system of the microscope had about a 80% efficiency. Therefore, assuming spherically symmetric emission, the light reaching the PD represented about 0.2% of the total emitted light. Using the PD responsivity of 0.2 A/W at 500 nm [21] as shown in Fig. 4, and assuming a photocurrent in the PD, I_{PD}, of 0.5 nA the total light emitted by the LED would be about 1 μW.

In another series of measurements, the PD-B set-up was used where a circular PD with a diameter of 9 mm and a 2.7 mm hole in the middle was mounted on a fixture as shown in Fig. 5. The fixture was attached to the objective of the microscope so that the distance from the PD to the LED was 5 mm. Accurate positioning of the LED was possible because it was visible through the hole in the detector. With this PD-B set-up the light collected from the LED in FM was several times

Downloaded From: https://www.spiedigitallibrary.org/conference-proceedings-of-spie on 1/29/2019
Terms of Use: https://www.spiedigitallibrary.org/terms-of-use

higher than with the PD-A set-up whereas in AM the values were very similar. This was correlated to the fact that the PD with positioning PD-B collected relatively more infrared (IR) light than with PD-A.

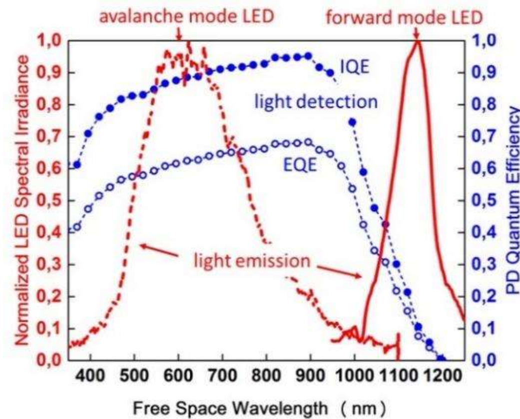

Figure 4. Normalized light emission spectra for a PureB LED operated in either AM or FM, and the external and internal quantum efficiency of a PureB photodiode detector with a 3-nm-thick PureB-only light-entrance window.

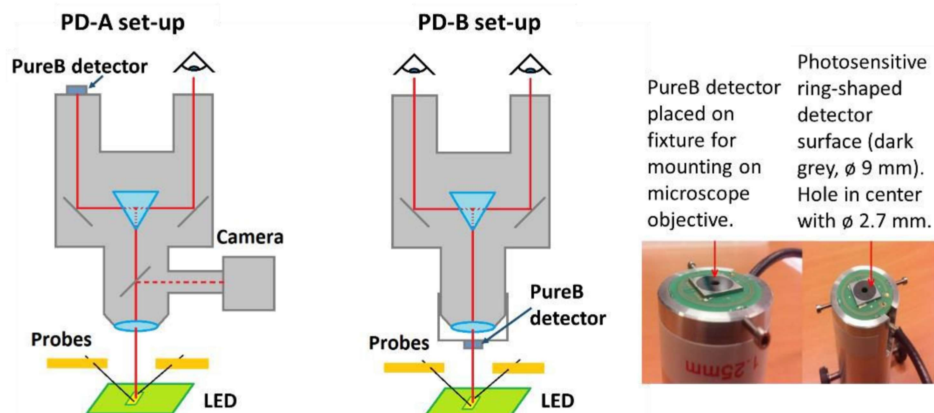

Figure 5. Schematics of the 2 set-ups for on-wafer biasing and monitoring of the light emission from the PureB LEDs. Left: PD-A set-up with the PureB detector connected one of the oculars of the binocular microscope. Middle: PD-B set-up with the PureB detector placed on a fixture to the objective Right: Photographs of the PureB detector on the fixture for mounting on the microscope objective.

All measurements were performed at ambient temperature that varied from 22ºC to 26ºC. This had no noticeable effect on the emitted light intensity but resulted in a PD dark current, I_{dark}, variation from 1.2 nA to 1.6 nA. The PD current generated by the emitted light, I_{PD}, was often about this amount so to assure a good accuracy each measurement point was repeated 10 times. The dark current was continuously monitored and subtracted from the measured PD current, $I_{PD,meas}$ to obtain the desired photocurrent generated by the emitted LED light, $I_{PD} = I_{PD,meas} - I_{dark}$.

Lastly, images of the light emission from the LED surface were made using a camera mounted on the microscope as shown in the PD-A set-up in Fig. 5. A cooled XENICS XEVA-257 camera was used for the visible spectrum of the AMLEDs and an XEVA-320 InGaAs camera for the near IR spectrum of the FMLEDs and each image was integrated over a duration of 20 s.

3. RESULTS AND DISCUSSION

In all the 3 different types of devices, both SPAD-quality and high dark-current devices were found, but the amount of the latter was larger in the D2[nn$^-$] devices and practically always present in the D3[nn$^+$n$^-$] devices. For the small D1[pn$^+$n$^-$]

Downloaded From: https://www.spiedigitallibrary.org/conference-proceedings-of-spie on 1/29/2019
Terms of Use: https://www.spiedigitallibrary.org/terms-of-use

devices, up to about 8 μm in size, almost all had SPAD-quality *I-V* characteristics, examples of which are reported in [20, 23] and some results are shown in Fig. 6. The larger devices mainly exhibited signs of early impact ionization events so possibly some very small density of defects was also playing a role in these devices. For the D2[nn$^-$] and D3[nn$^+$n$^-$] devices the large anode sizes were characterized by a variety of breakdown characteristics with high dark currents, examples of which are shown in Fig. 7. Many of the curves displayed jumps in the reverse current that occur once or twice in the course of the whole reverse bias sweep up to the *BV*. The number of devices displaying such jumps and the level of associated high dark currents increased as the n-enhancement doping increased. This is to be expected because the depletion width will be reduced which also entails an increase in the electric field. In Fig. 6 it is seen that the ideal *BV* set by the doping profiles decreases from 14 V to 11 V for the 40 keV implant going from 1×10^{12} cm^{-2} to 8.5×10^{12} cm^{-2}.

In addition to the current jumps, the presence of defects in the high dark-current devices was identified as light spots in the images of diodes operated with high reverse biasing. Examples are shown in Fig. 8 where a SPAD-quality D2[nn$^-$] device is compared to a D3[nn$^+$n$^-$] device characterized by a large current jump at 7 V reverse biasing. Such jumps around 5 V-7 V were typical for both the small and large D3[nn$^+$n$^-$] devices and light-emission spots appeared when the reverse voltage was above 7 V. The light intensity from each spot became higher and the number of visible spots increased with the applied voltage. Finally, the spots at the outer edge of the anode would join to form a bright ring. As opposed to this, for the SPAD-quality devices, no spots were visible and a uniform, very slightly granular, emission was observed for biasing above the

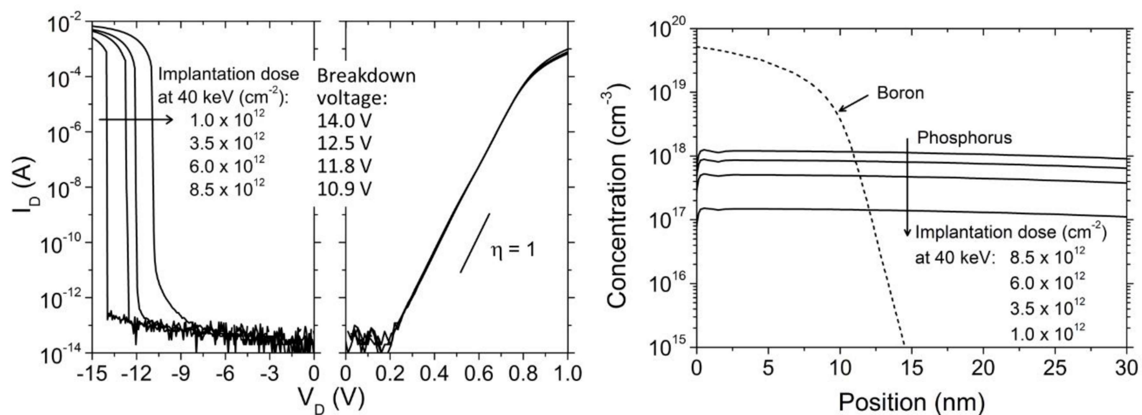

Figure 6. Left: Measured *I-V* characteristics for SPAD-quality diodes reported in [21] for 4 different 40 keV P$^+$ n-enhancement implantations. The diodes have a diameter of 4 μm. The breakdown voltages corresponding to the n-enhancement dose are also noted. Right: Simulations of the p$^+$n doping-profiles of the boron diffused from the PureB deposition and the annealed P$^+$ n-enhancement implantations [20].

14 V *BV*. This can originate from small non-uniformities in the n-doping that modify the electric field. As for the devices with spots, the outer ring also became brighter than the central area as the reverse bias increased. The formation of the bright outer rings could be correlated to the lateral series resistance through the p-region of the PureB anode. With a sheet resistance of 1.7 kΩ/sq, it is low enough to not be significantly depleted by the reverse biasing voltages but high enough to cause crowding of the LED current when it increases to values above 10 μA. As the current increases to mA levels, the current crowding was so strong that the LED perimeter emission accounted for most of the photocurrent produced in the PD. Another possible explanation for this behavior is that there might be a second breakdown higher than the *BV* set by the n-enhancement implantation, at the anode perimeter. It was shown by simulations that the high curvature at the edge of the PureB diode p-region could result in an electric field strength large enough to cause such a second breakdown [22].

In FM operation no clear spots were seen and the light emission was uniform until at high voltages an IR glow a few micrometer around the anode formed. This wide, glowing ring can be understood in terms of the wavelengths around 1100 nm that comprise the forward bias spectrum. For a forward bias of 5 V, the whole surface of the anode was bright with a glowing ring a few micrometer around the anode. The strong IR glow around the anodes in FM shows that the confinement of the light is better in AM where only visual light is emitted. It has been suggested that this would also be an advantage of the AM operation of the LED since it could result in less optical crosstalk.

Downloaded From: https://www.spiedigitallibrary.org/conference-proceedings-of-spie on 1/29/2019
Terms of Use: https://www.spiedigitallibrary.org/terms-of-use

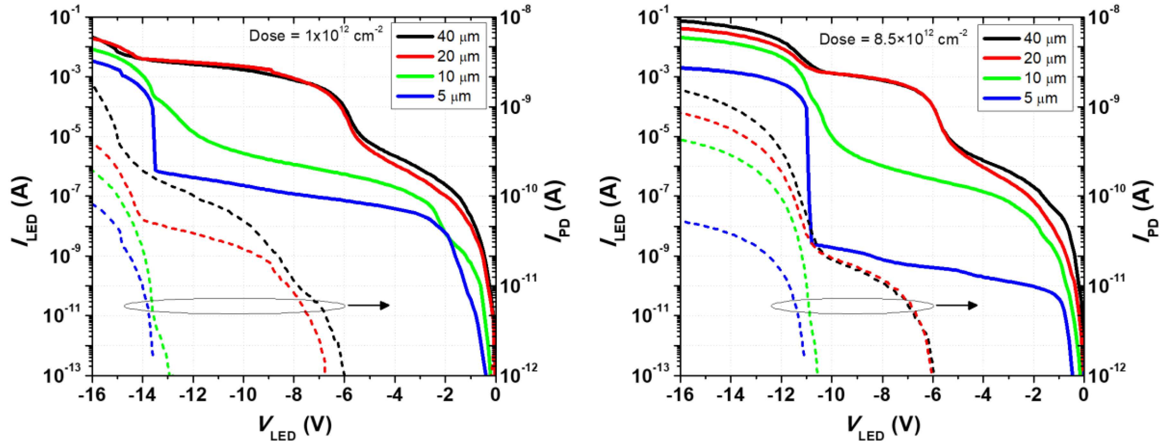

Figure 7. I_{LED}-V_{LED} characteristics and photodiode current I_{PD} measured with set-up PD-B for circular D2[n⁻n] LEDs with diameters 5 µm, 10 µm, 20 µm, and 40 µm, and a 40 keV n-enhancement dose of 1×10^{12} cm^{-2} (left) and 8.5×10^{12} cm^{-2} (right).

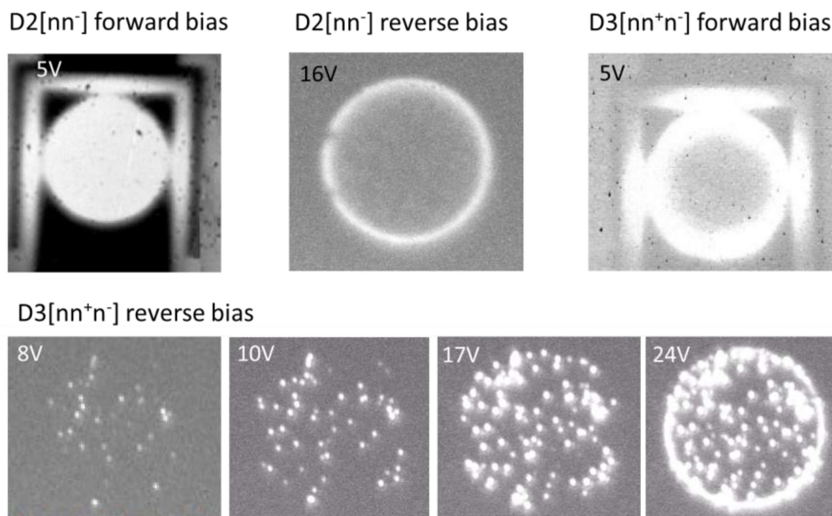

Figure 8. Camera images of the light emission from forward and reverse biased circular D2[nn⁻] and D3[nn⁺n⁻] diodes with a diameter of 40 µm. The applied bias voltage is given in each image.

In Fig. 7 the photocurrent I_{PD} measured in reverse with the PD-B set-up is plotted along with the LED current, I_{LED}, as a function of the LED biasing voltage, V_{LED}. The jumps in I_{LED} are accompanied by a clear increase in I_{PD} if the voltage is above about 5 V. The I_{PD} has the most significant increase above the 14 V BV, but above 5 V the electric field, E_f, is apparently high enough to set off avalanching events that result in significant light emission. The defects in the Si lattice are a source of g-r centers that in first instance increase the dark current. If the E_f becomes high enough, early impact ionization events can occur. At even higher E_f, self-quenching avalanche events and finally sustained avalanching with diode breakdown will follow. Thus, the defects can be viewed as a source of extra carrier injection into the depletion region that can lower the effective BV. Attempts were made to match the light spots on these devices to abnormalities on the anode surface that could be caused by, for example, stacking faults in the epitaxial layer. However, neither optical nor scanning-electron microscopy revealed any irregularities. In [12] the light emission spectra in AM were analyzed and fitted to an analytical model for the spectral light-emission dependence on the electric field strength. A diode with 14 V BV was compared to one with significant I_{LED} and associated light emission starting at 7 V. The latter had a small shift of the spectrum to shorter wavelengths as shown in Fig. 9. This was predicted by the analytical model [12] where the primary dependence of emission spectrum was assumed to be on the hot carrier temperature which was derived from the effective electric field.

Downloaded From: https://www.spiedigitallibrary.org/conference-proceedings-of-spie on 1/29/2019
Terms of Use: https://www.spiedigitallibrary.org/terms-of-use

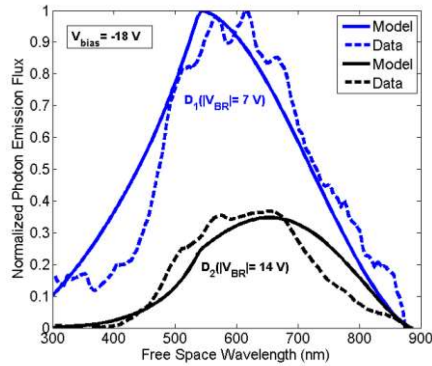

Figure 9. Comparison between measured (dashed) and predicted (bold) spectral variation in photon emission flux at a reverse bias of 18 V for a D2[nn$^-$] diode with BV = 14 V and a D3[nn$^+$n$^-$] diode with BV = 7 V, as reported in [12].

The light emission from the D2[nn$^-$] and D3[nn$^+$n$^-$] devices was measured for a large number of device geometries using the PD-A set-up. In Fig. 10 the I_{LED} is plotted as a function of V_{LED} for 40-µm-wide rectangular devices with lengths from 0.5 µm to 20 µm. In reverse, the current level in the D3[nn$^+$n$^-$] diodes is about 2-3 times higher than in the D2[nn$^-$] diodes. This is directly related to the current jumps that, even on this linear I_{LED} scale, are visible at V_{LED} = 7 V. The D2[nn$^-$] diodes display a clear BV at 14 V, at which voltage the most narrow D3[nn$^+$n$^-$] diodes display a kink in the current increase with voltage, indicating that the 14 V breakdown is now appreciably supplementing the current generated by defect-related light spots. The largest device, with $L \times W = 40 \times 20$ µm^2, does not display such a kink, presumably because the defect count was high and the current initiated by these many defects was dominating. When comparing all the devices, the reverse avalanche currents increased with both voltage and diode width as would be expected. However, the I_{LED} increase with width follows the perimeter rather than the area. This is in accordance with the current crowding effect identified also from the images of the light emission as discussed above.

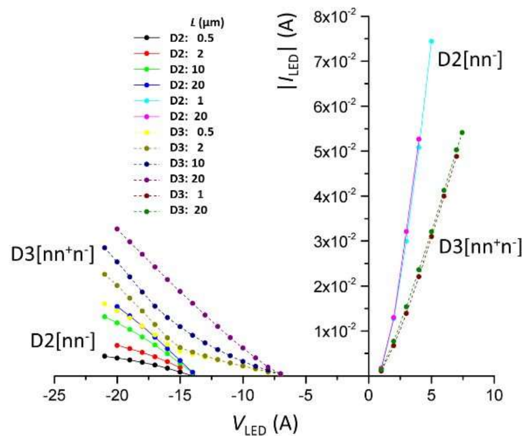

Figure 10. Set-up PD-A measurements of I_{LED} as a function of V_{LED} plotted on lin-lin scale for rectangular D2[n$^-$n] and D3[nn$^+$n$^-$] LEDs all with W = 40 µm and L = 0.5 µm, 1 µm, 2 µm, 10 µm, or 20 µm. The 40 keV n-enhancement dose is 1×10^{12} cm^{-2}.

In FM operation, the D2[nn$^-$] diodes have a much higher I_{LED} than the D3[nn$^+$n$^-$] diodes, and it is independent of the width of the diodes. This can be understood in terms of the series resistance of the cathode contact which was made on the back of the wafer to the n-type substrate. Therefore, the forward current was predominantly attenuated by the series resistance through the substrate. The effective series resistance was found to about 500 Ω, extracted from the lin-lin diode I-V characteristics as the slope of the high current regions that all converged to the same linear characteristic. Therefore, all diode geometries resulted in almost the same high voltage current. However, the D3[nn$^+$n$^-$] devices with a buried n$^+$-layer had a lower I_{LED}. The presence of this highly-doped layer, that is characterized by a high Gummel number and much lower

Downloaded From: https://www.spiedigitallibrary.org/conference-proceedings-of-spie on 1/29/2019
Terms of Use: https://www.spiedigitallibrary.org/terms-of-use

carrier mobility and lifetimes, reduces the spreading of the holes injected in to the n-substrate and the chance of light-emitting recombination events.

The dependence of I_{PD} on I_{LED} and power dissipation, $P_{LED} = I_{LED} \times V_{LED}$, for rectangular and circular devices are compiled in Fig. 11 for both AM and FM operation of the LED. While the I_{LED} increases with device area/perimeter, the I_{PD} behaves less regularly. One source of spread in this connection was the varying surroundings of the devices on-wafer. The metallization and probe-needles reflected the emitted light to different degrees in the different devices. Nevertheless, the spread was so small that it does not hinder a comparison of the light emission levels from the different types of devices. Although the D3[nn$^+$n$^-$] diodes in AM started emitting light at about 7 V and have higher I_{LED} currents for the same voltage as the D2[nn$^-$] devices, there is little difference between the I_{PD} in the 2 cases as a function of I_{LED} or P_{LED} but there is a higher spread in the values. In contrast, in FM the D3[nn$^+$n$^-$] devices emit very little light with an I_{PD} of less than 0.02 nA while the D2[nn$^-$] devices have about the same increase in I_{PD} as a function of I_{LED} or P_{LED} as in AM. There is, however, a clear difference between the rectangular and circular devices, with higher I_{PD} for the rectangular devices that have a higher P/A ratio in all cases.

A number of the measurements were also performed with the PD-B detector. The results are shown in Fig. 12 for I_{PD} as a function of I_{LED} and P_{LED} for a large number of rectangular diodes. As mentioned in Section 2.2, the I_{PD} for FM operation of the LED was higher than that measured with the PD-A set-up whereas the AM results were about the same. This allowed a more clear measurement of the performance of the diodes with a buried n$^+$-layer in FM. A comparison was also made between D1[pn$^+$n$^-$] diodes with a 40 keV n-enhancement implant of either 1×10^{12} cm^{-2} or 6×10^{12} cm^{-2}. The additional reduction of the spreading of the holes injected into the substrate in FM when the n-substrate wafer is replaced by a p-substrate wafer is evident as a small reduction of the $I_{PD}(I_{LED})$ but for $I_{PD}(P_{LED})$ the values are about the same. Changing to a higher n-enhancement implantation, did not have any significant influence on the resulting I_{PD}, neither in FM nor AM. Although the change in BV from 14 V to 11V does give a small increase in E_f that should increase the LED current, this may be compensated by the increase in the Gummel number of the n-region that in FM will lower the hole injection into this region.

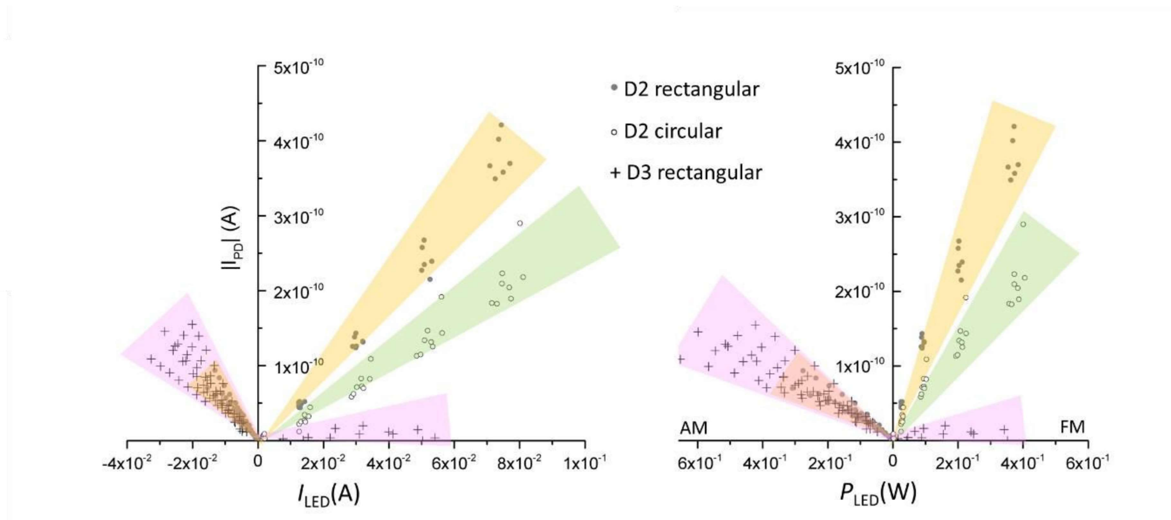

Figure 11. Set-up PD-A measurements of I_{PD} as a function of I_{LED} (left) and P_{LED} (right) for a large number of rectangular D2[n$^-$n] and D3[nn$^+$n$^-$] LEDs all with W = 40 µm and L going from 0.5 µm to 20 µm, and circular D2[n$^-$n] LEDs with diameters from 15 µm to 40 µm. The 40 keV n-enhancement dose is 1×10^{12} cm^{-2}.

The results are summarized in Table 2 and Table 3 in terms of the rate of increase of I_{PD} with I_{LED} and P_{LED}, $|\Delta I_{PD}/\Delta I_{LED}|$ and $|\Delta I_{PD}/\Delta P_{LED}|$, respectively. The spread in the rates is indicated by noting minimum and maximum values along with the average value.

Downloaded From: https://www.spiedigitallibrary.org/conference-proceedings-of-spie on 1/29/2019
Terms of Use: https://www.spiedigitallibrary.org/terms-of-use

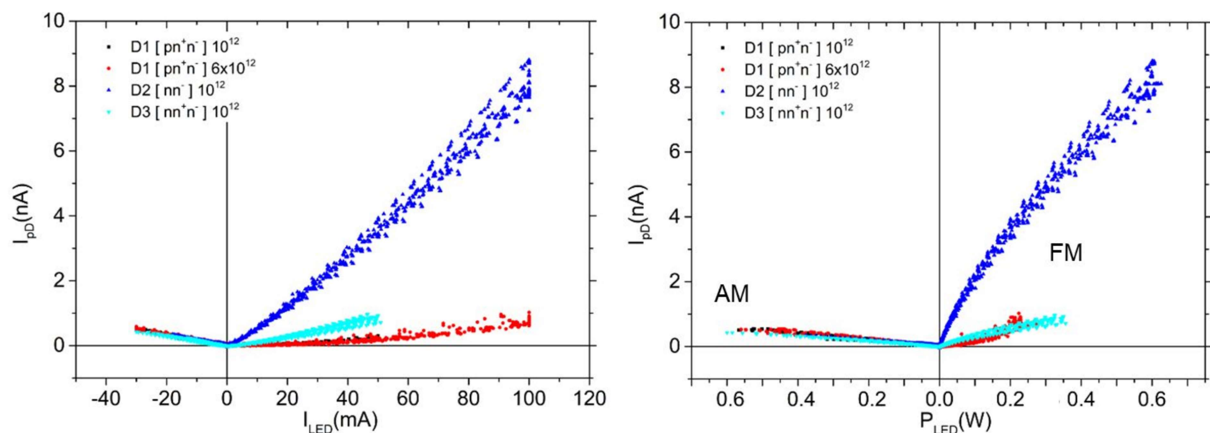

Figure 12. Set-up PD-B measurements of I_{PD} as function of I_{LED} (left) and P_{LED} (right) for a large number of rectangular D1, D2 and D3 LEDs with an n-enhancement dose of 1×10^{12} cm^{-2}. D1 diodes with a dose of 6×10^{12} cm^{-2} are also included.

Table 2. Overview of the rate of increase of of I_{PD} with I_{LED} and P_{LED} when the LED is operated in forward mode, as measured on a large number of diode geometries.

diode type	FM set-up	40 keV n-implant (atoms-cm^2)	$\|\Delta I_{PD}/\Delta I_{LED}\|$ ($\times10^{-10}$)			$\|\Delta I_{PD}/\Delta P_{LED}\|$ ($\times10^{-10}$ V^{-1})		
			average	min	max	average	min	max
D1[p$^-$n$^+$n]	PD-B	1×10^{12}	88	88	88	36	36	36
		6×10^{12}	96	84	122	41	33	49
D2[n$^-$n] circular	PD-A	1×10^{12}	28	21	36	8	5	11
	PD-B	1×10^{12}	-	-	-	-	-	-
D2[n$^-$n] rectangular	PD-A	1×10^{12}	48	40	56	13	11	16
	PD-B	1×10^{12}	860	770	930	130	120	140
D3[n$^-$n$^+$n]	PD-A	1×10^{12}	3	0	6	1	0	2
	PD-B	1×10^{12}	170	150	240	26	20	32

Table 3. Overview of the rate of increase of of I_{PD} with I_{LED} and P_{LED} when the LED is operated in avalanche mode, as measured on a large number of diode geometries.

diode type	AM set-up	40 keV n-implant (atoms-cm^2)	$\|\Delta I_{PD}/\Delta I_{LED}\|$ ($\times10^{-10}$)			$\|\Delta I_{PD}/\Delta P_{LED}\|$ ($\times10^{-10}$ V^{-1})		
			average	min	max	average	min	max
D1[p$^-$n$^+$n]	PD-B	1×10^{12}	176	176	176	10	10	10
		6×10^{12}	183	183	183	9	9	9
D2[n$^-$n]	PB-A	1×10^{12}	56	44	69	3	2	4
	PD-B	1×10^{12}	235	235	235	9	9	9
D3[n$^-$n$^+$n]	PD-A	1×10^{12}	54	32	76	3	2	4
	PD-B	1×10^{12}	151	151	151	7	7	7

Downloaded From: https://www.spiedigitallibrary.org/conference-proceedings-of-spie on 1/29/2019
Terms of Use: https://www.spiedigitallibrary.org/terms-of-use

4. CONCLUSIONS

The presented results where light emission from Si PureB LEDs was monitored with a Si PureB photodiode detector, support previously drawn conclusions that for on-chip optocoupling in Si, operation as AMLED may be preferable to the FMLED option. One of the pertinent advantages of the AMLEDs is the much lower charge storage of the LED upon reverse biasing, which is determined by the requirements of circuit speed. With respect to light coupling, the present results demonstrate that although the light emitted in FM only has a small spectral overlap with the detector, the I_{PD} is potentially higher than what can be obtained in AM. However, a suitable device design for this may not be possible in a circuit situation because of the speed requirements. In the presented LEDs this meant that due to demands for low series resistance and component isolation, the anode was surrounded by highly-doped cathode regions that suppressed the spreading of the carriers injected from the anode into the substrate. This lowered the detected FMLED light emission to levels well below that of the same device operated as AMLED. For the ultrashallow PureB diodes studied here it was advantageous to use narrow rectangular anodes rather than circular shapes to achieve the highest LED current density, thus minimizing the effect of current crowding at the anode perimeter. Nevertheless, with respect to the dependence of the I_{PD} on the dissipated power P_{LED} in AM, there is no great difference between the different devices geometries and fabrication methods studied here. The presence of a low but significant density of defects was identified in some devices by early avalanching events and the appearance of light spots at voltages below the ideal breakdown voltage. These defects gave a larger spread in the I_{PD} to P_{LED} relationship but otherwise did not have any noteworthy beneficial effect on the I_{PD} level. In FM, defect-related behavior was not observed.

When purely looking at the steady-state light-emission levels as is done in this work, there is no compelling advantage of introducing defects in the processing of the LEDs. For application as SPADs it is clear that PureB technology is attractive because of the damage-free anode formation that can result in very low DCRs and very reliable breakdown voltages. However, for data transmission purposes, such low DCRs impede a fast triggering of avalanching events and the concurrent light emission. A small density of defects has been shown to be useful for achieving fast triggering but only as long as they do not entail such high leakage current that an abrupt transition from a low-current off-state to the high-current on-state is prevented. From our reported results it is apparent that the unintended introduction of defects during the processing lead to a wide spectrum of reverse I_{LED}-V_{LED} characteristics, some of which were suitable for on-off keying while others were not. This suggests that it is probably difficult to use defects as a reliable, reproducible manner of increasing the injection of carriers to increase the triggering probability of obtaining an avalanche event. Other methods of obtaining the necessary current injection from structures in the vicinity of the LED have been reported earlier [25-27] and some of these methods also promise a very substantial increase in the AM light emission. This was not achieved with the defect-related emission reported in the present work, particularly not when the defect density was low enough to allow reliable power-efficient on-off keying for data transmission.

.

ACKNOWLEDGEMENTS

The authors would like to thank Lin Qi and the staff of the former DIMES IC-processing line for the PureB device fabrication, and Sander Smits for assistance with building the opto-electrical measurement set-up. This work was partially funded by the Netherlands Organisation of Scientific Research (NWO) Domain Applied and Engineering Sciences, The Netherlands, under Projects 12835 and 13535.

REFERENCES

[1] Snyman, L.W., Aharoni, H., Biber, A., Bogalecki, A., Canning, L., du Plessis, M., and Maree, P., "Optical sources, integrated optical detectors, and optical waveguides in standard silicon CMOS integrated circuitry," Proc. SPIE, 3953, pp. 3953–3953–17, (2000).

Downloaded From: https://www.spiedigitallibrary.org/conference-proceedings-of-spie on 1/29/2019
Terms of Use: https://www.spiedigitallibrary.org/terms-of-use

[2] du Plessis, M., Aharoni, H., and Snyman, L.W., "Silicon LEDs fabricated in standard VLSI technology as components for all silicon monolithic integrated optoelectronic systems," IEEE J. Sel. Topics Quantum Electron., 8(6), pp. 1412–1419, (2002).

[3] Huang, B., Zhang, X., Wang, W., Dong, Z., Guan, N., Zhang, Z., and Chen, H., "CMOS monolithic optoelectronic integrated circuit for on-chip optical interconnection," Opt. Commun., 284, pp. 3924–3927, (2011).

[4] Dutta, S., Hueting, R.J.E., Agarwal, V., and Annema, A.-J., "An integrated optical link in 140 nm SOI technology," Proc. Conference on Lasers and Electro-Optics (CLEO), Session JW2A, 132, (2016).

[5] Chatterjee, A., Bhuva, B.L., and Schrimpf, R.D., "High-speed light modulation in avalanche breakdown mode for Si diodes," IEEE Electron Device Letters, 25(9), pp. 628–630, (2004).

[6] Dutta, S., Agarwal, V., Hueting, R.J.E., Schmitz, J., and Annema, A.-J., "Monolithic optical link in silicon-on-insulator CMOS technology," Opt. Express, 25(5), pp. 5440–5456, (2017).

[7] Snyman, L. W., Aharoni, H., Biber, A., Bogalecki, A., Canning, L., du Plessis, M., and Maree, P., "Optical sources, integrated optical detectors, and optical waveguides in standard silicon CMOS integrated circuitry," Proc. SPIE, 3953, pp. 3953–3953–17, (2000).

[8] Agarwal, V., Dutta, S., Annema, A.-J., Hueting, R.J.E., Lee, M.-J., Charbon, E., and Nauta, B., "Optocoupling in CMOS", to be presented at IEEE Electron Devices Meeting (IEDM), (2018).

[9] Cova, S., Ghioni, M., Lacaita, A., Samori, C., and Zappa, F., (1996). "Avalanche photodiodes and quenching circuits for single-photon detection". Applied Optics, 35, pp. 1956–1976 (1996).

[10] Agarwal, V., Annema, A.-J., Dutta, S., Hueting, R.J.E., Nanver, L.K., and Nauta, B., "Random telegraph signal phenomena in ultrashallow p^+n avalanche diodes," IEEE J. Electron Devices Soc., 6(1), pp. 642–652 (2018).

[11] Agarwal, V., Annema, A.-J., Member, Hueting, R.J.E., Dutta, S., Nanver, L.K., and Nauta, B., "Data Transmission Capabilities of Silicon Avalanche Mode Light-Emitting Diodes", IEEE Trans. Electr. Dev., 65(11), pp. 4883-4890 (2018).

[12] Dutta, S., Hueting, R.J.E., Annema, A-J., Qi, L., Nanver, L.K., and Schmitz, J., "Opto-electronic modeling of light emission from avalanche-mode silicon p^+n junctions", J. Appl. Phys., 118, p. 114506 (2015).

[13] Nanver, L.K., Qi, L., Mohammadi, V., Mok, K.R.M., de Boer, W.B., Golshani, N., Sammak, A., Scholtes, T.L.M., Gottwald, A., Kroth, U. and Scholze, F., "Robust UV/VUV/EUV PureB Photodiode Detector Technology With High CMOS Compatibility," IEEE J. Selected Topics in Quantum Electronics 20(6), 306–316 (2014).

[14] Qi, L., and Nanver, L.K,, "Conductance along the interface formed by 400°C pure boron deposition on silicon", IEEE Electron Device Letters,Vol. 36(2), pp.102-104 (2015).

[15] Šakić, A., Nanver, L.K., Van Veen, G., Kooijman, K., Vogelsang, P., Scholtes, T.L.M., de Boer, W., Wien, W.H.A., Milosavljević, S., Heerkens, C.T.H., Kneževic, T., and Spee, I., "Versatile silicon photodiode detector technology for scanning electron microscopy with high-efficiency sub-5 keV electron detection," Proc. IEEE Electron Devices Meeting (IEDM), 31-4, pp. 712-716 (2010).

[16] Lee, M.-J., Ximenes, A.R., Padmanabhan, P., Wang, T.-J., Huang, K.-C., Yamashita, Y., Yaung, D.-N., and Charbon, E., High-Performance Back-Illuminated 3D-Stacked Single-Photon Avalanche Diode Implemented in 45 nm CMOS Technology," IEEE J. Selected Topics in Quantum Electronics, 24(6), p. 3801809, (2018).

[17] Nanver, L.K., Lyon, K., Liu, X., Italiano, J., and Huffman, J., "Material Reliability of Low-Temperature Boron Deposition for PureB Silicon Photodiode Fabrication," MRS Advances, 3(57-58), (Electronic and Photonic Materials), pp. 3397-3402, (2018).

[18] Charbon, E., "Towards large scale CMOS single-photon detector arrays for lab-on-chip applications," J. Phys. D, Appl. Phys., 41-9, p. 094010 (2008).

[19] Villa, F., Lussana, R., Bronzi, D., Tisa, S., Tosi, A., Zappa, F., Dalla Mora, A., Contini, D., Durini, D., Weyers, S., and Brockherde, W., "CMOS imager with 1024 SPADs and TDCs for single-photon timing and 3-D time-of-flight," IEEE J. Sel. Topics Quantum Electron., 20(6), p. 3804810, (2014).

[20] Q. L., Mok, K. R. C., Aminian, M., Charbon, E., and Nanver, L.K., "Fabrication of Low Dark-Count PureB Single-Photon Avalanche Diodes," 29th Sym. on Microelectron. Techn. and Devices (SBMicro), (2014).

Downloaded From: https://www.spiedigitallibrary.org/conference-proceedings-of-spie on 1/29/2019
Terms of Use: https://www.spiedigitallibrary.org/terms-of-use

[21] Qi, L., Mok, K.R.C., Aminian, M., Charbon, E. and Nanver, L.K., “UV-sensitive low dark-count PureB single-photon avalanche diode”, IEEE Trans. Electron Devices, 61(11), pp. 3768-3774 (2014).
[22] Knežević, T., Nanver, L.K., and Suligoj, T., "2D dark-count-rate modeling of PureB single-photon avalanche diodes in a TCAD environment," Proc. of SPIE, 10526(K), Physics and Simulation of Optoelectronic Devices XXVI, pp. 1-10, (2018).
[23] Qi, L., Sluyterman, S., Kooijman, K., Mok, K.R.C., and Nanver, L.K., “PureB single-photon avalanche diodes for low-energy electron detection down to 200 eV,” Optics Letters, 40(3), pp. 300-303 (2015).
[24] Snyman, L.W., du Plessis, M., and Aharoni, H., “Injection-avalanche based n^+pn silicon complementary metal–oxide–semiconductor light emitting device (450–750 nm) with 2-order-of-magnitude increase in light emission intensity”, Jpn. J. Appl. Phys. 46(4B), pp. 2474-2480 (2007).
[25] Snyman, L.W., du Plessis, M., and Bellotti, E., “Photonic transitions (1.4eV–2.8 eV) in silicon pþnpþ injection-avalanche CMOS LEDs as function of depletion layer profiling and defect engineering”, IEEE J. Quant. Elec., 46(6), pp. 906-919 (2010).
[26] Xu, K., “On the design and optimization of three-terminal light-emitting device in silicon CMOS technology”, IEEE J. Sel. Topics Quantum Electron., 20(4), (2014).

Downloaded From: https://www.spiedigitallibrary.org/conference-proceedings-of-spie on 1/29/2019
Terms of Use: https://www.spiedigitallibrary.org/terms-of-use